Check for updates

MATERIALS SCIENCE

Photovoltaic nanoassembly of nanowire arrays sensitized with colloidal nanocrystals for near-infrared retina photostimulation

Tarik S. Kaya[1]†, Humeyra N. Kaleli[2]†, Antoine Chaffiol[3]†, Andrea Corna[4], Corentin Joffrois[3], Ridvan Balamur[5], Ugur B. Caliskan[5], Asim Onal[6], Cigdem Pehlivan[2], Eren Tekinay[1], Alp Yilmaz[1], Roya Mohajeri[5], Arif E. Cetin[7,8], Günther Zeck[4], Serge Picaud[3], Sedat Nizamoglu[5]*

Copyright © 2026 The Authors, some rights reserved; exclusive licensee American Association for the Advancement of Science. No claim to original U.S. Government Works. Distributed under a Creative Commons Attribution NonCommercial License 4.0 (CC BY-NC).

Nanowires have served as a transformative platform for advanced neural and tissue interfaces. While their photovoltaic properties hold exceptional promise for neural modulation, existing photostimulation approaches predominantly rely on visible light–activated photoelectrochemical mechanisms. Here, we present a solution-processed photovoltaic nanoassembly comprising a ZnO nanowire array sensitized with $AgBiS_2$ nanocrystals that enables efficient near-infrared (NIR) neural stimulation through capacitive photocurrents. By optimizing nanowire morphology and nanocrystal interdigitation, the platform achieves high charge injection densities (tens of microcoulombs per square centimeter) at low NIR intensities (<1 milliwatt per square millimeter). The nanoassembly was subretinally placed in an ex vivo blind rat retina, where it elicited repeatable and robust responses in retinal ganglion cells under NIR pulses. Notably, these responses were achieved at light intensities substantially below established ocular safety limits. The nexus of neuronal systems and nanoassemblies offers potential for enabling unconventional visual prosthetics and advanced neuromodulation therapies.

INTRODUCTION

Nanowires (NWs) have emerged as a versatile nanomaterial platform for electrophysiology, enabling single-cell recordings (*1*), three-dimensional (3D) tissue mapping (*2*), and in vivo brain activity monitoring (*3*). Their unique potential extends to photovoltaic neural stimulation, where they convert light energy into bioelectrical signals to modulate neuronal activity (*4*, *5*). This capability stems from their high surface area–to–volume ratio, which enhances charge separation and collection, while their nanoscale geometry promotes exceptional light trapping and absorption (*6*). Such properties enable ultraefficient photovoltaic operation, even at the single-NW level (*7*).

Current silicon NWs (single or arrays) (*8*, *9*) and TiO_2 NW arrays (*10*) have demonstrated the ability to mediate photostimulation across biological scales from single cells to whole organs. Although these systems mainly operate through photoelectrochemical mechanisms, capacitive stimulation driven by electrode-electrolyte charging dynamics and regarded as the clinical gold standard for neural interfaces provides superior control and biocompatibility (*11*–*13*). Emerging strategies, including gold nanoparticle functionalization of TiO_2 NWs (*14*) and controlled oxygen vacancy engineering during growth (*15*), have shifted the photostimulation toward capacitive-dominated photocurrents. However, current strategies predominantly rely on visible light, even though infrared stimulation offers benefits, including greater tissue penetration and higher safety thresholds for light exposure (*16*–*20*).

Here, we demonstrate a photovoltaic nanoassembly composed of a ZnO NW array sensitized with $AgBiS_2$ nanocrystals (NCs) for near-infrared (NIR) photostimulation. The nanoassembly was optimized to maximize capacitive charge injection by tuning the NW length and interdigitating NC layer, which enables a high-performance photoresponse (tens of $\mu C\ cm^{-2}$) at low NIR intensities (<1 $mW\ mm^{-2}$). The nanoassembly enabled healthy and functional in vitro neuronal cultures without inducing intracellular stress, demonstrating its potential as a biocompatible optoelectronic interface for neural applications. The nanoassembly achieved reliable functional activation of the blind rat retina while operating below ocular safety limits. These findings highlight the potential of this nanoassembly as a safe and efficient interface for next-generation retinal prosthetics and infrared neuromodulation.

RESULTS

Device fabrication and operation

The device has a photovoltaic nanoassembly composed of ZnO NWs and $AgBiS_2$ NCs as the stimulation electrode and a pseudocapacitive layer of ruthenium oxide (RuO_2) as the return electrode. For the nanoassembly fabrication, we followed a multistep process that mainly included the vertical growth of the ZnO NW array and interpenetration of NCs (Fig. 1A). We started the fabrication of the solution-processed photovoltaic nanoassembly by forming a 30-nm ZnO seed layer onto indium tin oxide (ITO), and we grow the ZnO NW arrays via chemical bath deposition, which can be controlled within the range of 90 to 350 nm by adjusting the duration of the chemical bath deposition (fig. S1). We selected to grow ZnO NWs with a mean length of 240 nm on the seed layer and an average interspacing of 30 nm (Fig. 1, B and C). As the photoabsorption layer, we selected $AgBiS_2$ NCs because of their exceptional absorption coefficient reaching over $10^5\ cm^{-1}$, high photostability, and being free from toxic heavy metals such as cadmium and lead (fig. S2). ZnO

[1]Department of Materials Science and Engineering, Koc University, Istanbul, Turkey. [2]Research Center for Translational Medicine, Koc University, Istanbul, Turkey. [3]Sorbonne Université, CNRS, INSERM, Institut de la Vision, F-75012 Paris, France. [4]Institute of Biomedical Electronics, TU Wien, Vienna, Austria. [5]Department of Electrical and Electronics Engineering, Koc University, Istanbul, Turkey. [6]Department of Biomedical Science and Engineering, Koc University, Istanbul, Turkey. [7]Izmir Biomedicine and Genome Center, Izmir 35330, Turkey. [8]Department of Biophysics, Faculty of Medicine, Dokuz Eylul University, Izmir 35340, Turkey.
*Corresponding author. Email: snizamoglu@ku.edu.tr
†These authors contributed equally to this work.

Downloaded from https://www.science.org at Koc Universitesi Suna Kirac on July 02, 2026

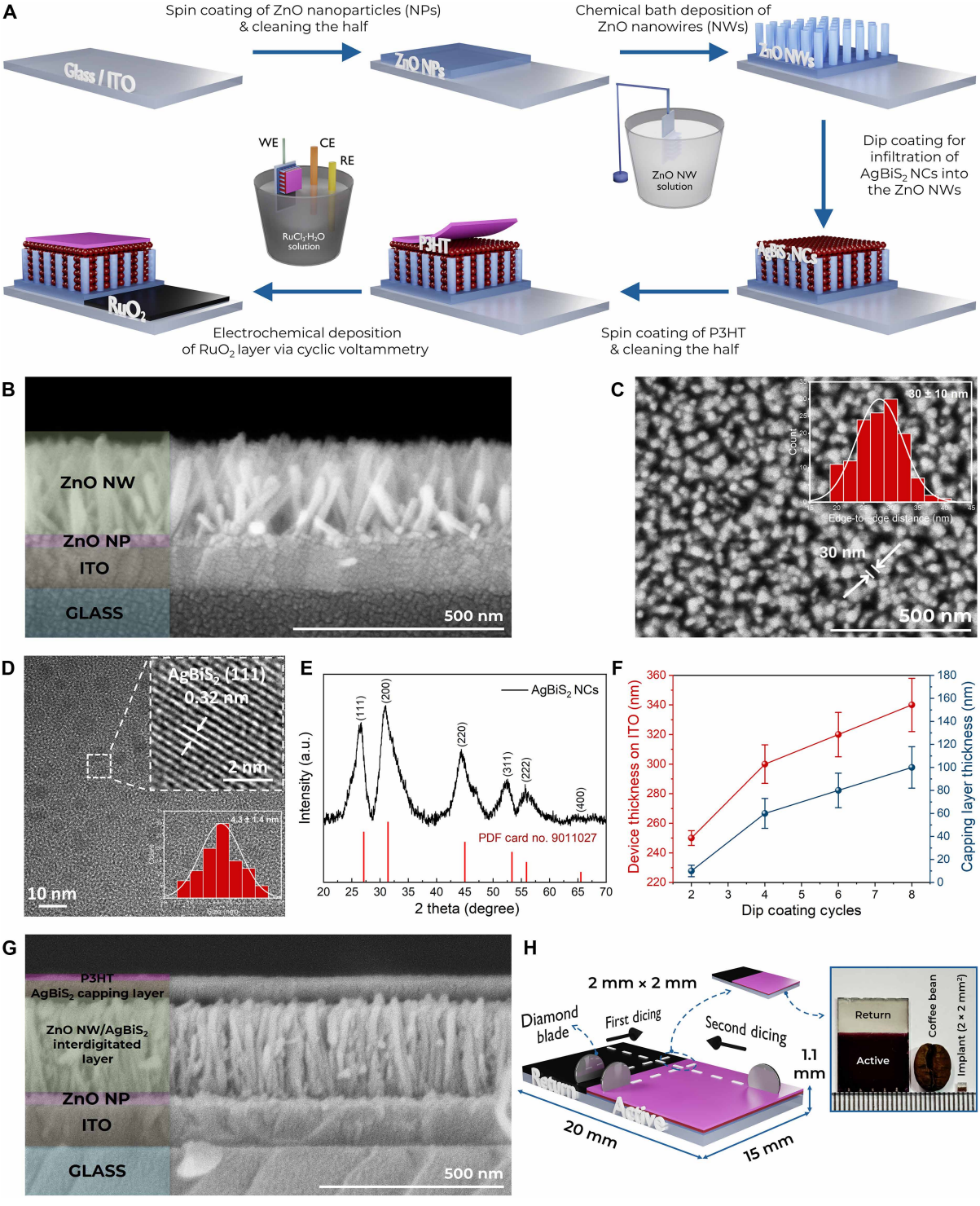


Fig. 1. Device fabrication and operation. (**A**) Fabrication flow schematic of the photovoltaic nanoassembly (not drawn in scale). (**B**) Cross-sectional scanning electron microscope image of ZnO NWs. (**C**) Scanning electron microscope image of the top view of ZnO NWs (the inset is the edge-to-edge distance of the ZnO NW distribution histogram and the calculated average distance). (**D**) TEM and high-resolution TEM (HRTEM) images of $AgBiS_2$ NCs. The inset shows the NC size distribution histogram and the calculated average size (4.3 ± 1.4 nm). (**E**) XRD pattern of $AgBiS_2$ NCs. (**F**) $AgBiS_2$ layer thickness versus implemented dip coating cycles. (**G**) Cross-sectional scanning electron microscope image of the nanoassembly. (**H**) Schematic illustration of the dicing process of the nanoassembly and optical images of the photovoltaic nanoassembly both before and after the dicing process, next to a coffee bean. The distance between each bar represents 1 mm.

Downloaded from https://www.science.org at Koc Universitesi Suna Kirac on July 02, 2026

and $AgBiS_2$ form a proper type II heterojunction for dissociation of the photogenerated charges for the photovoltaic process. The synthesis of colloidal $AgBiS_2$ NCs was done by using a hot injection method (fig. S3) on the basis of the reaction of silver(I) acetate [Ag(OAc)], bismuth(III) acetate [$Bi(OAc)_3$], and hexamethyldisilathiane solution dissolved in 1-octadecene (ODE) as the sulfur source that yielded a mean NC size of 4.3 ± 1.4 nm (Fig. 1D). The x-ray diffraction (XRD) pattern of the $AgBiS_2$ NCs revealed a rock salt crystal structure (Fig. 1E), and the average size estimation using the Scherrer equation (~4.2 nm) was also in close agreement with transmission electron microscopy (TEM).

Subsequently, NCs were introduced into the ZnO NWs by using a layer-by-layer deposition technique, which allows for precise control of the thickness of the interdigitated NC layer (Fig. 1F). Given that the electron diffusion length in $AgBiS_2$ is limited around 60 nm, which is much shorter than the hole diffusion length (150 nm) (*21*), ZnO NWs facilitate effective charge dissociation via interpenetration within the $AgBiS_2$ NCs (*22*). Then, tetramethylammonium iodide (TMAI) was applied to exchange long-chain insulating oleate ligands with small-chain iodide ions to enhance the electronic coupling between the NCs. X-ray photoelectron spectroscopy (XPS) showed the removal of oleates by a shift toward higher binding energies originating from Ag 3d (367.8 and 373.8 eV) and Bi 4f (157.9 and 163.2 eV) (fig. S4). The successful ligand exchange was further confirmed by Fourier transform infrared spectroscopy (FTIR) by the disappearance of oleate absorption bands characteristic of —CH2— and —CH3— functional groups (2850 to 2960 cm^{-1}) (fig. S5). The thickness of the capping layer (NC thickness above the NW array) is adjusted to 80 nm (Fig. 1G), which can be well controlled by changing the dip coating cycle (figs. S6 and S7). Afterward, a water-stable and biocompatible polymer of poly 3-hexylthiophene (P3HT) with a thickness of 30 nm was deposited as the hole transport layer to complete the photoactive part of the photovoltaic nanoassembly. For the formation of the return electrode, 40 cycles of electrodeposition of the RuO_2 layer with a thickness of 72 ± 13 nm (fig. S11) are done via cyclic voltammetry (CV) on the bare ITO side of the device to enhance the electrode-electrolyte capacitance.

Photoelectrochemical characterization

We did photoelectrochemical characterization in artificial cerebrospinal fluid (aCSF), which has the nanoassembly as the working electrode under light irradiation, Ag/AgCl as the reference electrode, and platinum as the counter electrode (Fig. 2A). To understand the charge-injection characteristics of the photovoltaic nanoassembly, we fabricated a series of devices with varying NW lengths in combination with different cycles of NC deposition (Fig. 2B). The photocurrent increases with NW length up to about 240 nm, after which the performance drops rapidly with further extension. Using 240-nm ZnO NWs, the photovoltaic nanoassembly generated maximum photocurrent and photovoltage values of 3.27 mA cm^{-2} and 350 mV with an 80-nm capping layer (i.e., six cycles of dip coating) (Fig. 2C) under NIR illumination (λ = 780 nm, 89 mW cm^{-2}), respectively (Fig. 2, D and E). The charge injection density corresponded to 20.96 ± 2.2 μC cm^{-2} (mean ± SEM, n = 10) (Fig. 2F), which is sufficiently high to meet the needed thresholds for in vivo stimulation (*13*) and 20 times higher than the device without the RuO_2 layer. Moreover, before the ligand exchange, the device only generated a photocurrent of 0.26 mA cm^{-2} (fig. S8) and a charge density of 3.6 μC cm^{-2}, while replacing the insulating oleate ligands with compact iodide ligands via TMAI treatment significantly enhanced interparticle electronic coupling and surface passivation, thereby improving charge transport across the NC film (*23*). The observed symmetric and quasi-rectangular shapes of the cyclic voltammograms of RuO_2 reveal the capacitive behavior of the films and the presence of reversible redox reactions, which is the preferred mechanism for safe neurostimulation (figs. S9 and S10). The cathodic charge storage capacity of RuO_2 was 15.3 ± 2.1 mC cm^{-2}, and the capacitance corresponded to 31.2 ± 1.2 mF cm^{-2} (mean ± SEM, n = 10).

We also quantified the photoresponse of the nanoassembly under various illumination conditions. The charge injection by the nanoassembly can be modulated by light intensity (Fig. 2G) and pulse duration (Fig. 2H). For example, under a short pulse duration (1 ms, 89 mW cm^{-2}), the photovoltaic nanoassembly delivers 2.52 ± 0.5 μC cm^{-2} (mean ± SEM, n = 10) (Fig. 2H), which falls within the threshold range required to stimulate various neural tissues, such as the auditory brainstem and subthalamic nucleus (*13*). The experimental and simulated absorption spectra for different dip coating cycle numbers, along with the real (n) and imaginary (k) parts of the refractive index of the materials, were used as the optical constants for the finite-difference time-domain (FDTD) simulations (figs. S12 and S13). FDTD simulations show that the localized electromagnetic fields with extensive intensity enhancements are finely confined along the ZnO NW interstices for effective photogeneration (Fig. 2I). Moreover, our analysis into the photoresponse at varying wavelengths (Fig. 2J) revealed a larger photocurrent for 450- and 625-nm light illumination than the NIR illumination, which can be attributed to the absorption of blue light by the P3HT layer and the enhanced oscillator strength of $AgBiS_2$ NCs at shorter wavelengths.

Last, we assessed the photoelectrical properties of the nanoassembly under a freestanding and wireless retina implant condition. For that, the nanoassembly was diced into a 2 mm–by–2 mm size (Fig. 1H). The nanoassembly was immersed in aCSF, and a glass capillary counter electrode and remote Ag/AgCl reference electrode were used in voltage-clamp mode using a patch pipette filled with an intracellular solution positioned near the biointerface surface (Fig. 2K). The nanoassembly exhibited a peak photocurrent of 2.7 ± 0.2 nA at the position indicated by the blue circle under NIR illumination (λ = 780 nm, 2 mW mm^{-2}). Moreover, the photocurrent distribution was mapped by varying the position of a patch pipette from the stimulation electrode to the return electrode. A reversal of the photocurrent was observed, which was attributed to anodic current at the stimulation electrode caused by hole-triggered photocurrent flowing from the surface to the electrolyte and cathodic current at the return electrode (Fig. 2L). The spatial selectivity of the devices was evaluated by directly measuring the interfacial photocurrent at the electrode-electrolyte interface (fig. S14). The photocurrent amplitude decreased to 75% of its peak value at the edge of the illuminated spot and further dropped to 46% at a distance of 150 μm. This decay indicates that the photocurrent spread is well localized within the illuminated area.

Photoelectrical stability and biocompatibility

To evaluate the photoelectrical stability of the photovoltaic nanoassembly, we measured its photoresponse after subjecting the devices to accelerated reactive aging, low-temperature sterilization, and repeated photoexcitation. For accelerated aging, they were incubated at 87°C in an H_2O_2-supplemented aCSF environment. Charge injection performance was assessed at 48-hour intervals, corresponding

Downloaded from https://www.science.org at Koc Universitesi Suna Kirac on July 02, 2026

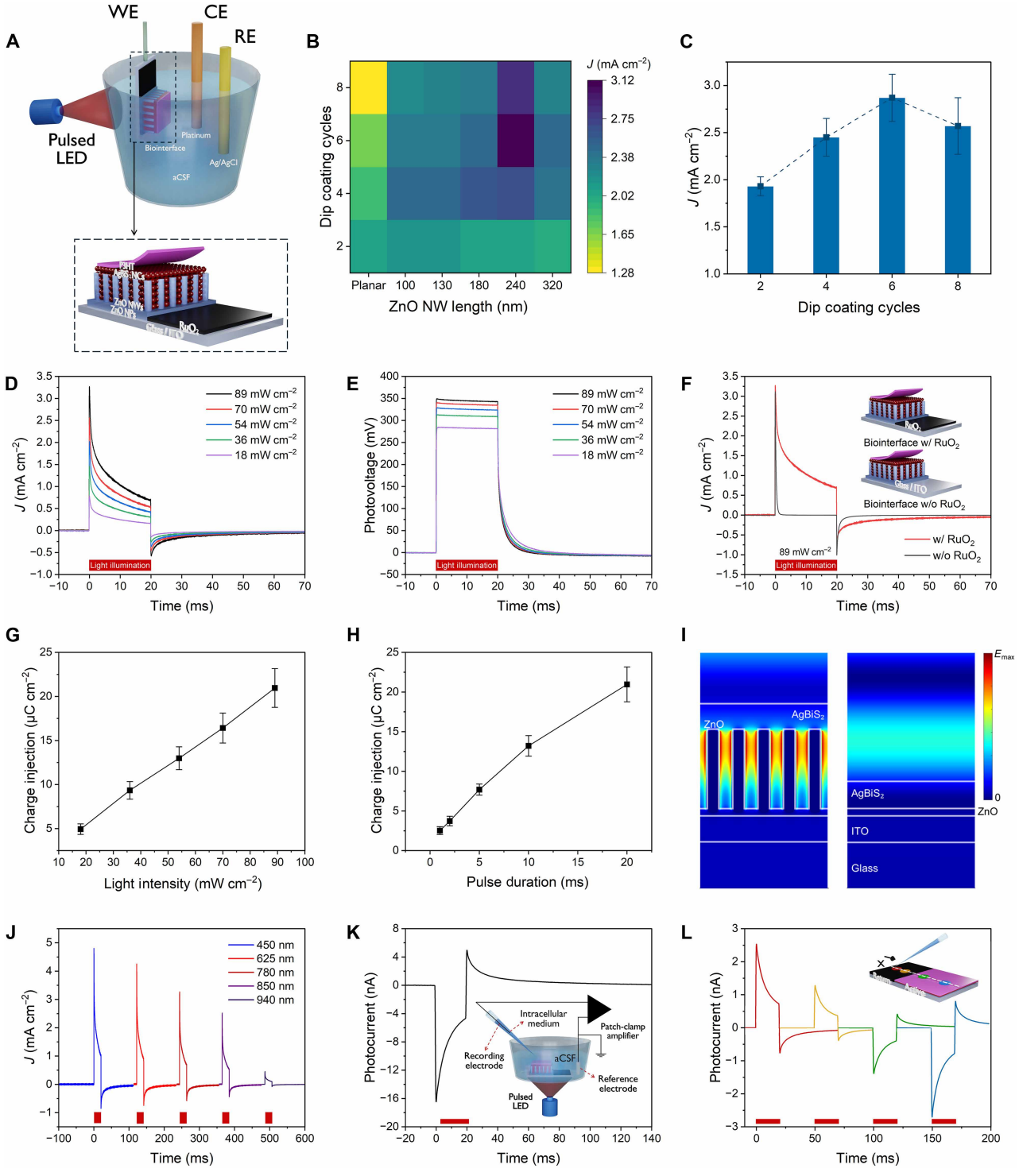


Fig. 2. Photoelectrochemical characterization. (**A**) Schematic illustration of the three-electrode potentiostat for photocurrent and photovoltage measurement. (**B**) Photocurrent density of the nanoassemblies with different NW length and NC deposition combinations. (**C**) Photocurrent density for different dip coating cycles under NIR light illumination (mean ± SD, $n = 10$). (**D**) Photocurrent density and (**E**) photovoltage of the biointerface after RuO_2 integration under different light intensity levels ($\lambda = 780$ nm). (**F**) Photocurrent density of the nanoassembly with and without RuO_2 under the illumination of 89 mW cm^{-2}. The inset demonstrates the illustration of the measured devices. (**G**) Charge injection of the nanoassembly as a function of light intensity. (**H**) Photogenerated charge injection of the nanoassembly for different pulse durations. (**I**) Near-field intensity distribution of the nanoassembly (left) demonstrating strong electromagnetic field localization between NWs compared to the NW-absent case (right). (**J**) Photocurrent response as a function of illumination wavelength. (**K**) Photocurrent of the nanoassembly characterized by using a patch-clamp setup. The inset demonstrates the schematic of the setup. (**L**) Photocurrent profile of the nanoassembly after the dicing process as a function of the x axis. The inset shows the measurement system, where the circles designate as the patch pipette position.

Downloaded from https://www.science.org at Koc Universitesi Suna Kirac on July 02, 2026

to a simulated aging period of 2 months, and after a 24-month equivalent aging period, the biointerface retained 79 ± 7% of its initial charge injection performance (Fig. 3A). Low-temperature sterilization—comprising ethanol rinsing, ultraviolet (UV) sterilization, overnight incubation in cell culture medium, and a second ethanol rinse—did not significantly alter photoelectrical properties, with 87 ± 2% of charge injection and 83 ± 3% of photovoltage preserved (Fig. 3B). Photostability under repeated excitation (20,000 illumination cycles) was also confirmed, with the biointerface maintaining 84 ± 9% of its initial charge injection (Fig. 3C).

For biocompatibility assessment, primary hippocampal neurons cultured on the nanoassembly or control ITO substrates (Fig. 3D) were evaluated for viability and cytotoxicity using CellTiter-Glo (CTG), 3-(4,5-dimethylthiazol-2-yl)-2,5-diphenyltetrazolium bromide (MTT), and lactate dehydrogenase (LDH) assays. The CTG assay, which measures adenosine 5′-triphosphate levels as an indicator of metabolic activity, revealed comparable viability between the device and control groups (Fig. 3E). The MTT assay indicated higher metabolic activity in neurons cultured on the nanoassembly (Fig. 3F), while LDH leakage confirmed no membrane integrity compromise or cytotoxicity (Fig. 3G). Immunofluorescence staining (NeuN for nuclei and β-III tubulin for the cytoskeleton) at days 0 and 14 demonstrated sustained neuronal viability and characteristic morphology on the biointerface, with no significant differences in cell distribution compared to controls (Fig. 3H). Total cell counts followed similar trends, confirming the nanoassembly's compatibility with long-term neuronal culture (fig. S15).

To assess oxidative stress and mitochondrial function, intracellular reactive oxygen species (ROS) were monitored using H_2DCFDA (2′,7′-dichlorodihydrofluorescein diacetate), a cell-permeant fluorescent probe that is cleaved by ROS to generate emissive DCF (2′,7′-dichlorofluorescein). Neurons exposed to 10,000 illumination cycles (780 nm, 5 Hz, 20-ms pulse width, 1.5 mW mm^{-2}) showed no significant ROS increase compared to ITO controls, whereas H_2O_2-treated positive controls exhibited elevated fluorescence (Fig. 3I). The mitochondrial membrane potential (MMP), a key indicator of mitochondrial health, was assessed using JC-1. Healthy mitochondria retain JC-1 as red aggregates, while depolarized mitochondria exhibit green monomers. After light stimulation (780 nm, 5 Hz, 20-ms pulse width, 1.5 mW mm^{-2}), no significant shift in the aggregate-to-monomer ratio was observed (fig. S16).

NIR photostimulation of P23H blind rat retina

To demonstrate the potential of the photovoltaic nanoassembly for restoring visual function, we evaluated its ability to evoke neural activity in the degenerated retina of a blind rat model (P23H), a well-established model for inherited blindness characterized by early photoreceptor degeneration. The retinal explant was placed onto a microelectrode array (MEA) with the photovoltaic implant positioned on the opposite side of the retina, facing the inner nuclear layer (Fig. 4A). This is one of the standard experimental conditions used to test the PRIMA implants under preclinical trials (*24*). Full-field NIR light pulses were delivered using a 880-nm light source, a wavelength at which ocular transmittance is high (~80%) and photoreceptor sensitivity is extremely low, which is about 10^{-7} relative to the normalized peak sensitivity at 555 nm (*25*). The first step of the analysis involved removing stimulation artifacts from the filtered MEA recordings to ensure more accurate spike detection (Fig. 4A). Of the 13 animals tested with the implants, 6 experiments were performed under conditions in which both the spontaneous retinal activity remained stable for a sufficient duration and the implant-retina contact was tight enough to elicit significant neuronal responses to NIR stimulation (along with positive-polarity saturating artifacts). We observed that robust neural activation of retinal ganglion cells (RGCs) following NIR stimulation (Fig. 4B) and spatial mapping of RGC responses (Fig. 4C) revealed localized activation, with higher response amplitudes observed in regions of the MEA in proximity to the photovoltaic nanoassembly part generating anodic photocurrents. Examples of mean firing responses from individual units (Fig. 4D) demonstrated time-locked spiking activity with high temporal precision following stimulation onset.

To investigate the impact of NIR pulse width on retinal responses, we quantified RGC activity across multiple retinas stimulated with varying pulse durations (5, 10, 20, and 50 ms). Because laser stimulation saturates MEA sites, spikes occurring during the stimulation period are not detectable in our recordings, which directly affects the shape of the observed response profiles. As shown in Fig. 5 (A and B) in a representative retina, shorter pulses already elicited high firing rates and activated a greater number of responsive units compared to longer pulses (20 to 50 ms). Shorter pulse widths (5, 10, and 20 ms) produced significantly higher peak firing rates (compared to 50 ms). With the shortest pulses (5 ms) where we believe that most elicited spikes were captured (outside of the short blind window of saturation), the measured response peak latency was very fast (13.38 ± 0.95 ms, mean ± SEM, $n = 38$ units). Considering the duration of the saturation periods, we additionally quantified the peak response time with respect to the end of each stimulation pulse (fig. S17). Together, responses across all tested retinas (Fig. 5C, $N = 6$ retinas) showed that, on average, 20% of active sites responded to NIR stimulation, with 10-ms pulses yielding the highest peak firing rates (81.83 ± 14.51 Hz, mean ± SEM, $N = 6$ retinas). Control experiments using retinas without implants showed no significant activity under identical stimulation conditions (no responsive sites, $N = 3$ retinas), confirming that the observed responses were specific to photovoltaic stimulation (Fig. 5D).

These results demonstrate that short NIR pulse durations (~5 to 10 ms) enable robust retinal activation, likely due to an already efficient charge injection. Shorter pulses are also preferable for minimizing potential photodamage and thermal effects. Moreover, the light intensity at 2.27 mW mm^{-2} at 880 nm remained below the safety threshold of the light intensity for retina applications (fig. S18). To verify the thermal safety of the stimulation, temperature dynamics under 15 min of pulsed illumination (λ = 880 nm, 2.26 mW mm^{-2}, 20-ms pulses at 5 Hz) were recorded using a thermal camera. The temperature rise on the device surface was less than 0.1°C (fig. S19), consistent with values reported in the literature (*26*). The observed temporal precision and fast response kinetics were achieved with full-field device stimulation. In addition, to determine the threshold level for irradiance, a retina was stimulated with 10-ms laser pulses at three different irradiance levels. Of the eight responsive units identified at 2.27 mW mm^{-2}, all remained responsive at 1.44 mW mm^{-2}, and one unit still responded at 0.54 mW mm^{-2} (fig. S20). For comparison, in the PRIMA (*24*) study, in vitro threshold irradiances were reported around 0.5 − 1 mW mm^{-2} under full-field stimulation in primate retinas. Although our dataset is smaller and the experimental models (blind rat versus primate retina) as well as the data analysis approaches differ, the ex vivo thresholds appear to be within a relatively similar range. Together, these results demonstrate

Downloaded from https://www.science.org at Koc Universitesi Suna Kirac on July 02, 2026

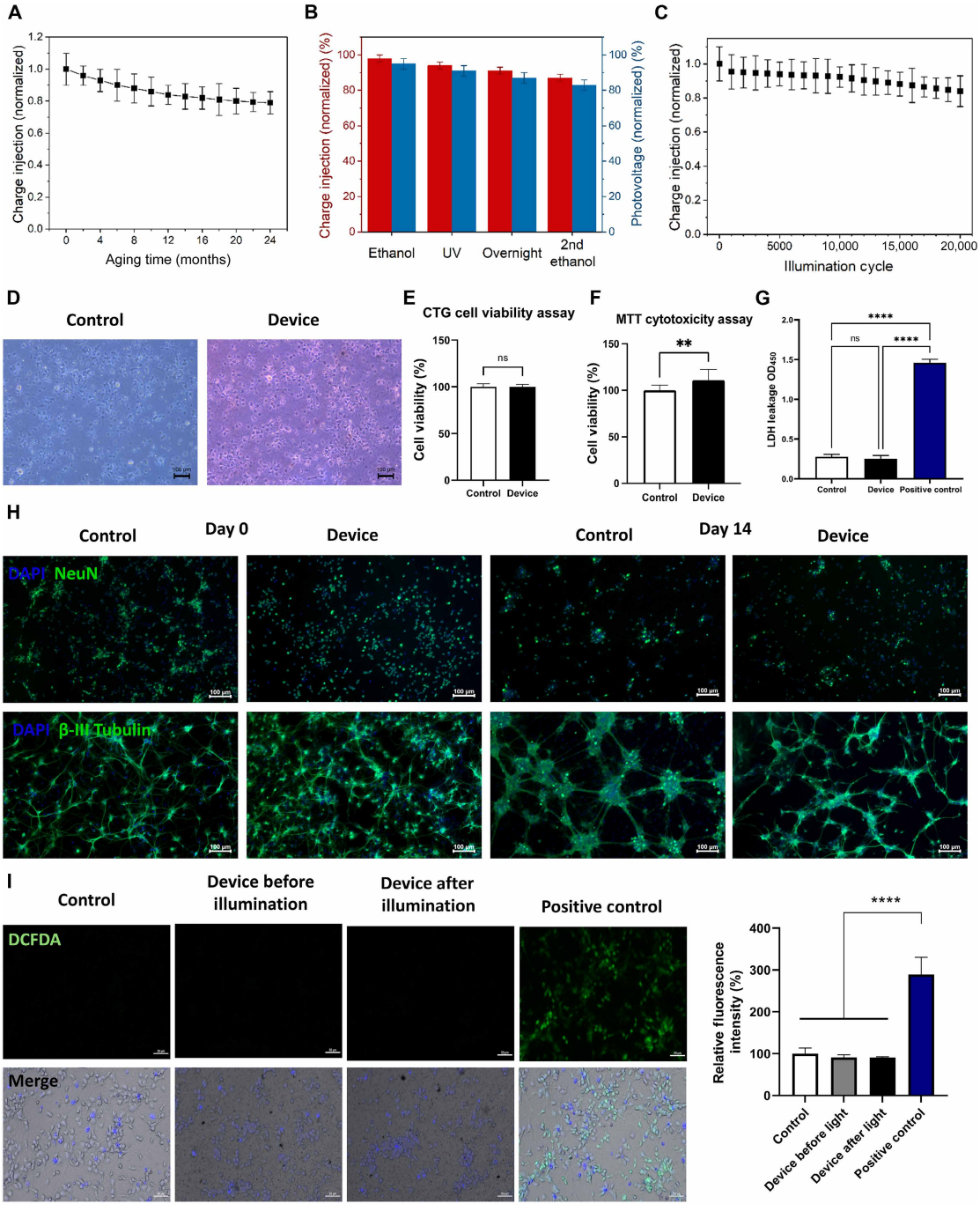


Fig. 3. Photoelectrical stability and biocompatibility. (**A**) Charge injection for different aging times. (**B**) Normalized photovoltage and charge injection after the sterilization steps. (**C**) Photocyclic stability of the interdigitated structure of the nanoassembly, assessed by monitoring the variation in charge injection over 20,000 photocycles. (**D**) Bright-field images of cells at 3 days in vitro (scale bar, 100 μm). (**E**) CTG assay for quantifying cell viability through the cellular adenosine 5′-triphosphate level in primary hippocampal neurons cultured on the ITO control and the biointerface device (mean ± SD, $n = 4$). The ITO sample was used as a control. (**F**) MTT assay for measuring the cytotoxicity of primary hippocampal neurons cultured on the ITO control and the device (mean ± SD, $n = 4$). (**G**) LDH leakage assay for measuring the cell membrane integrity of neurons on the substrates (mean ± SD for $n = 4$). The level of significance was calculated using an ordinary one-way analysis of variance (ANOVA); $^*P < 0.05$ was evaluated as statistically significant (ns, $P > 0.05$; $^{**}P < 0.01$; and $^{****}P < 0.0001$). (**H**) Short- and long-term neuron culture on the control and the device. Cells were costained with the DAPI (blue) nuclear marker and anti-NeuN (green) neuronal nuclear marker or anti–β-III tubulin (green) neuronal structure marker (scale bar, 100 μm). (**I**) Evaluation of intracellular oxidative stress with ROS assay after subjecting to 780-nm light with 10,000 cycles, illumination at a 5-Hz stimulus frequency, 20-ms pulse width, and 1.5 mW mm^{-2} optical power density. ITO is the negative control, and ITO with H_2O_2 is the positive control (scale bar, 50 μm). The fluorescence intensity of negative control is normalized to 100%. An ordinary one-way ANOVA was carried out to determine the statistical significance of the differences among multiple groups, and $^*P < 0.05$ was evaluated as statistically significant (ns, $P > 0.05$; $^{**}P < 0.01$; and $^{****}P < 0.0001$).

Downloaded from https://www.science.org at Koc Universitesi Suna Kirac on July 02, 2026

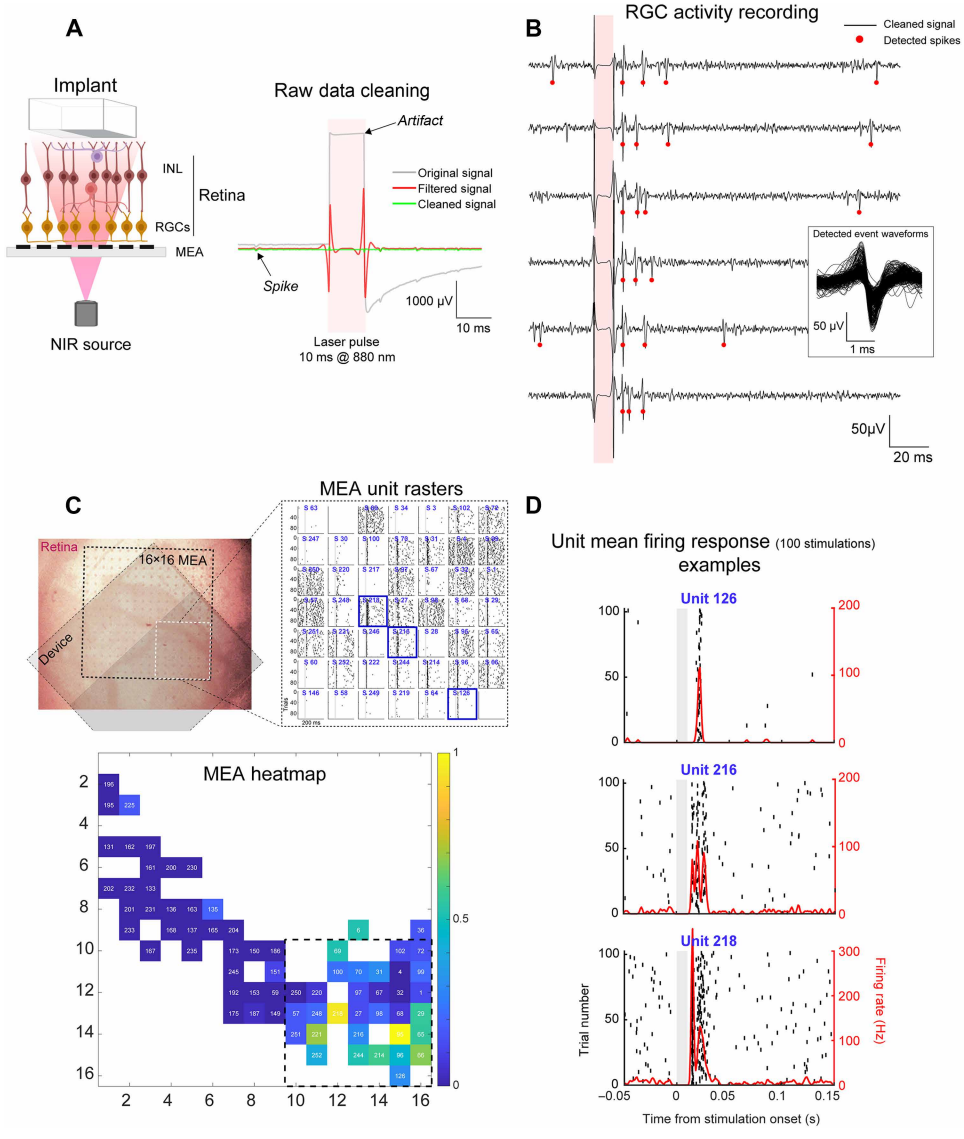


Fig. 4. Electrophysiological recordings from a blind rat retinal explant coupled with the photovoltaic device during NIR light stimulations. (**A**) Schematic representation of the experimental setup and raw data cleaning. A NIR light source (λ = 880 nm) stimulates the retinal explant through a photovoltaic implant placed on the retinal surface (left). The RGCs are recorded using a 16-by-16 MEA. The raw data undergo cleaning (right) to remove artifacts caused by laser stimulation. The original signal is represented in gray, the filtered signal in red, and the cleaned signal in green. INL, inner nuclear layer. (**B**) Representative recording from NIR stimulation replicates (data from one MEA unit). Cleaned signals are shown with detected spikes marked by red dots. The inset displays the waveforms of all detected events (from 100 replicates). Increased spiking activity is clearly visible following laser pulses. (**C**) Spatial mapping of retinal responses. Top left: Infrared image of the retinal explant positioned over the 16-by-16 MEA grid, with the device represented in gray. Top right: Raster plots (black dots) showing spiking activity across multiple units during repeated stimulations (dotted white square area from the top left). The vast majority of units are responsive and respond robustly in this area. Bottom: Spatial heatmap illustrating the normalized response amplitude across units [between 0 (dark blue for nonresponsive units) and 1 (yellow for the unit presenting the max response)], with higher responses localized to the bottom right region of the MEA. (**D**) Examples of raster plots and mean firing rates (red curves) from three individual units over 100 stimulation trials, demonstrating robust and time-locked responses to NIR stimulation onset.

the capability of the device to safely, effectively, and reliably activate retinal neurons ex vivo.

DISCUSSION

Retinal degenerative diseases are among the leading causes of vision loss worldwide, and with the aging global population, it is estimated that these conditions will affect 300 million people by 2040. Now, no definitive clinical treatment exists to prevent or cure these diseases once they develop. While companies like Alpha IMS and Argus II have discontinued their retinal implant technologies, photovoltaic retina implants (i.e., PRIMA) hold high promise for providing artificial vision to patients with retinal degenerative diseases (*27*, *28*). These implants convert incoming infrared radiation, which is not detected by the damaged photoreceptors, into subretinal photostimulation. For that, silicon photodiode–based implants were mainly

Downloaded from https://www.science.org at Koc Universitesi Suna Kirac on July 02, 2026

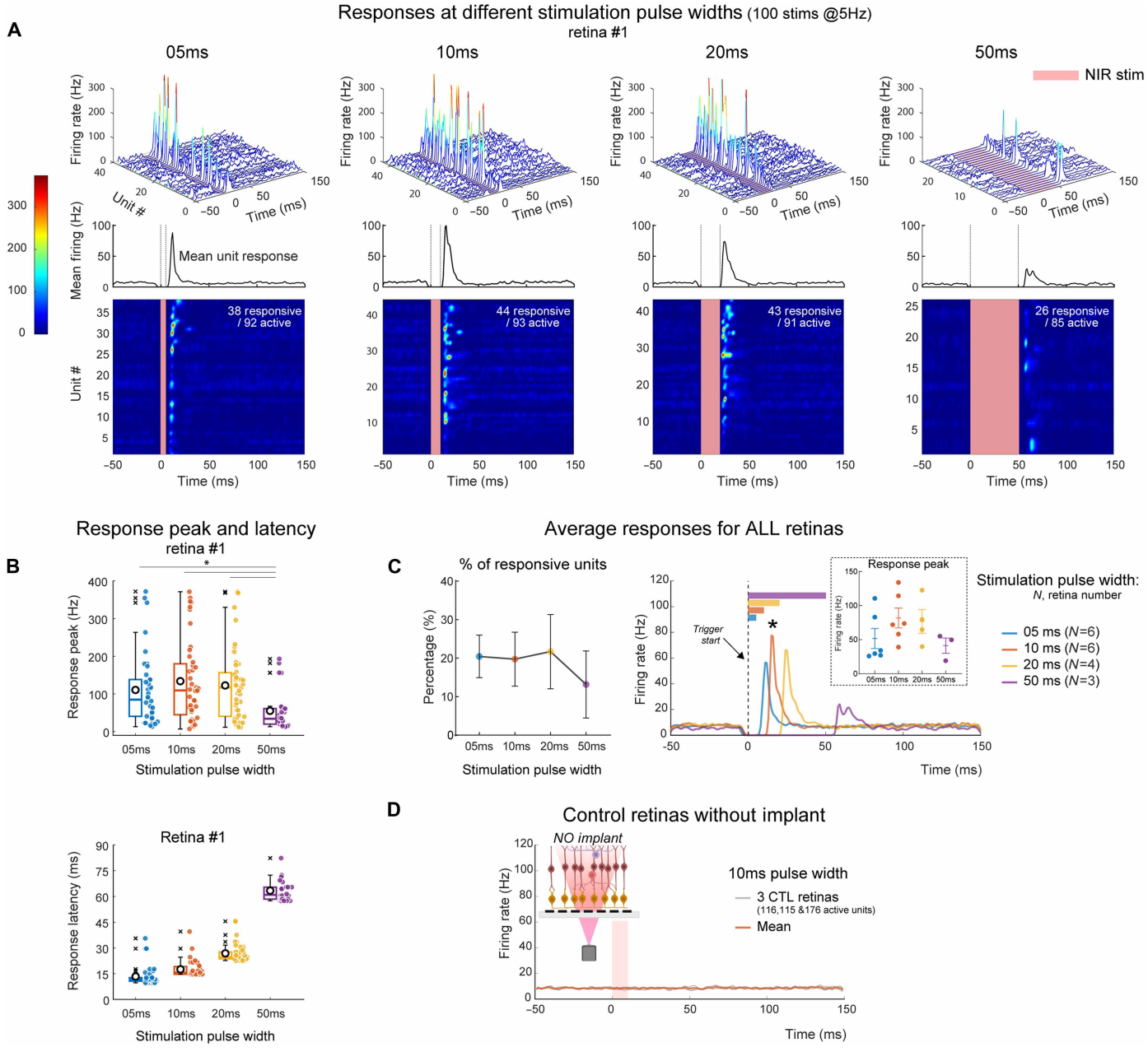


Fig. 5. Effect of NIR stimulation duration on retinal responses and controls in rat retina. (**A**) Responses of a representative implanted retina to four NIR pulse widths (5, 10, 20, and 50 ms). Top: Firing rate 3D plots for all responsive units. Middle: Average firing rate across units. Bottom: Heatmaps showing activity over time, with the number of active and responsive units indicated. Short pulses (≤ 20 ms) evoke strong, time-locked responses, while longer pulses reduce the number of detectable responsive units resulting from the extended laser artifact. (**B**) Quantification of response peak and response latency for the same retina. Box plots (black circles indicate the mean value) and individual data points show higher peaks and shorter latencies for shorter pulses. Statistics were performed using a Kruskal-Wallis test followed by multiple comparisons (*$P < 0.05$). (**C**) Average responses across all retinas. Left: Percentage of responsive units (responsive/active × 100) as a function of pulse width (mean ± SEM). Right: Mean firing rate curves for each condition (*N*, number of retinas), highlighting the consistent responses at all tested pulse widths (with a peak at 10 ms marked with a black asterisk). Inset: Plot of response peaks across conditions (each dot represents a retina, and individual units firing peak values were calculated before averaging them) for all retinas (mean ± SEM). (**D**) Control recordings from blind rat retinas without the implant stimulated with 10-ms pulses show no detectable responses (three retinas: 116, 115, and 176 active units), confirming that NIR-evoked activity requires the photovoltaic implant. All experiments were performed at a constant light intensity of 2.27 mW mm^{-2}.

Downloaded from https://www.science.org at Koc Universitesi Suna Kirac on July 02, 2026

preferred for effective retinal photostimulation. However, the low absorption coefficient of silicon in the NIR window requires a thick photoactive region (30 μm). Instead, the photovoltaic nanoassembly has a submicrometer (~0.5 μm) active device thickness that has high potential for translation toward large-area devices.

The key enabler of the photovoltaic nanoassembly is $AgBiS_2$ NCs, which are nontoxic, are composed of earth-abundant elements, and have a broad absorption spectrum spanning from the visible to NIR region, high air stability, and favorable solution processability (*29*). A particularly important feature of $AgBiS_2$ NCs is their high absorption coefficient (~10^5 cm^{-1}), which is substantially higher than the other NCs such as CdTe, GaAs, InP, and perovskites over a broad spectral range (400 to 1000 nm) (*30*, *31*). This high absorption coefficient allows for effective light absorption and thin device architectures while maintaining highly effective functionality.

Layer-by-layer assembly of nanomaterials is an adaptable and economical approach with nanoscale precision (*32*). It enables the deposition of nanocomponents onto various surfaces with complex geometries, such as the integration of NCs with NWs, as demonstrated in this study (*33*). This approach can further add advanced functionalities, including antimicrobial, wound healing, drug delivery, and tissue engineering capabilities (*34*). Moreover, beyond retina, the photovoltaic nanoassemblies show high promise for the application of a wide range of electrogenic tissues such as the heart, muscle, and brain (*35*–*37*).

Our photovoltaic device represents an advancement by combining four critical features for retinal implants: NIR operation, an ultrathin active electrode, high photoresponse, and wireless operation. Even though POLYRETINA shows thin and flexible devices, its operation is at the edge of the visible spectrum at 730 nm, where the ocular safety limits are lower. On the other hand, PRIMA has a strong photoresponse at 880 nm, but the photoactive layer is relatively thick because of the low absorption coefficient of silicon. Hence, NCs offer thin photoactive layers, enabling flexible devices while showing an effective retinal photoresponse at 880 nm. In addition, the photovoltaic approach enables wireless operation, eliminating the need for internal electronics and cables required by the systems like Argus II and Alpha-IMS that makes the implant simpler as a single integrated device and easier surgical procedure. As summarized in table S1, the implant developed in this study demonstrates an efficient photoresponse within a submicrometer architecture, comparable to or exceeding that of previously reported photovoltaic devices, and thus represents a viable approach for next-generation retinal prosthetics.

In conclusion, this work establishes a high-performance photovoltaic nanoassembly on the basis of ZnO NWs sensitized with $AgBiS_2$ NCs as a safe and efficient platform for NIR neural stimulation. By leveraging capacitive charge injections and optimizing NW morphology and NC integration, the system achieves high charge injection densities at low NIR intensities. Demonstrated effectiveness in evoking retinal responses in ex vivo models of blindness highlights its potential for next-generation visual prosthetics and broader neuromodulation applications.

MATERIALS AND METHODS

Synthesis of $AgBiS_2$ NCs

$AgBiS_2$ NCs were synthesized using a Schlenk line with a hot injection technique. Briefly, 1544 mg (4 mmol) of $Bi(OAc)_3$ and 536 mg (3.2 mmol) of Ag(OAc) were weighed in a glovebox and added to a 100-ml three-necked round-bottom flask containing 24 ml of oleic acid and 15 ml of ODE. The flask was then sealed with rubber septa to prevent leakage. Subsequently, the reaction solution was increased to 70°C under a vacuum environment and pumped for 2 hours to form Bi and Ag oleates while removing oxygen and moisture. Then, the reaction atmosphere was switched to Ar, and 4 mmol of hexamethyldisilathiane solution dissolved in 5 ml of ODE was swiftly injected into the reaction mixture. An immediate color change to dark brown was observed upon the injection into the reaction mixture, suggesting the successful formation of $AgBiS_2$ NCs. Afterward, the heating mantle was discontinued, and the reaction mixture was allowed to cool rapidly in a water bath for ~5 min. Subsequently, the crude solution was stirred for 1 hour at room temperature. Light exposure to the reaction flasks was minimized throughout the process. $AgBiS_2$ NCs were purified via sequential precipitation. The crude solution was isolated after adding ethanol and centrifugation at 9600 rpm for 6 min. The precipitate was then redispersed and reprecipitated twice using toluene and ethanol. The purified $AgBiS_2$ NCs were lastly dispersed in toluene at a concentration of 20 mg/ml for the fabrication of bioelectronic interfaces.

Synthesis of ZnO NWs

ZnO NWs were synthesized using the chemical bath deposition technique on an ITO/ZnO seed layer (Ossila, S111) by immersing half of the substrate in a solution (ZnO NW solution) of deionized water containing hexamethylenetetramine (0.025 M), NH_3-H_2O (0.70 M), polyethyleneimine (0.06 M), and zinc nitrate hexahydrate (0.05 M). During the process, the ZnO NWs were grown and developed on the seed layer through the reaction occurring in the solution. Following the formation of ZnO NWs on the ZnO seed layer, which was carried out at a temperature of 90°C for varying growth durations, an annealing process was conducted at a temperature of 180°C.

Characterization of $AgBiS_2$ NCs

UV-visible (UV-Vis) absorption characterization of the synthesized $AgBiS_2$ NCs was performed using a Shimadzu UV-3600 UV-Vis-NIR spectrophotometer in solution. Standard quartz cuvettes with a 1-mm optical path were used for the absorbance measurements.

TEM and high-resolution TEM analyses were conducted using a Hitachi HT7800 operating at 100 kV and a FEI TALOS F200S transmission electron microscope with an accelerating voltage of 200 kV, respectively. For TEM analysis, sample preparation was performed by depositing a diluted (10 μl of a 1 mM $AgBiS_2$ NC) toluene solution onto a copper support grid. The average crystallite size of the $AgBiS_2$ NCs was determined by measuring the diameters of at least 100 NCs from nonaggregated regions of the sample.

XRD analysis was performed on $AgBiS_2$ (NCs) at room temperature using a Rigaku Miniflex x-ray diffractometer with Cu Kα radiation ($\lambda = 0.154$ nm) and a scan rate of 5° min^{-1}. The samples were prepared by drop-casting NCs dissolved in toluene onto 1 cm–by–1 cm silicon wafers. The wafers were subsequently heated to 100°C for 1 hour to evaporate the solvent. Analysis of the XRD pattern using the Scherrer equation revealed an average crystallite size for the $AgBiS_2$ NCs.

XPS analysis was carried out to characterize the surface composition of $AgBiS_2$ NCs before and following ligand exchange. Measurements were conducted under ultrahigh-vacuum conditions (base pressure: 1×10^{-10} mbar) using a Thermo Scientific K-Alpha surface analysis instrument equipped with Al Kα monochromatic

Downloaded from https://www.science.org at Koc Universitesi Suna Kirac on July 02, 2026

radiation (1486.7 eV). Binding energies were referenced to the C-C peak in the C 1s spectrum (284.6 eV) for accurate XPS data analysis. Sample preparation for XPS involved spin-coating a toluene solution containing $AgBiS_2$ NCs (20 g/liter) onto preheated ITO substrates (20 mm by 15 mm). The substrates were heated to 110°C and maintained at this temperature for 10 min to facilitate solvent evaporation under ambient conditions. A double spin-coating process was implemented, ensuring a layered film structure.

FTIR analysis was performed on $AgBiS_2$ NC films before and after ligand exchange using a Thermo Scientific iS50 FTIR Spectrophotometer. FTIR samples were prepared using the same technique as XPS sample preparation.

Biointerface fabrication

Photovoltaic nanoassembly was fabricated on glass or polyethylene terephthalate (PET) substrates coated with ITO. The glass/ITO (Ossila, S111) or PET/ITO (Sigma-Aldrich, 639 303) substrates underwent a thorough cleaning process. The cleaning procedure was performed in an ultrasonic cleaner system set at 50°C by immersing the substrates consecutively in tension-active agent (HELLMANEX III):deionized water (3 and 97% by volume, respectively) for 15 min, deionized water for 15 min, acetone for 15 min, and isopropanol for 15 min. Following this cleaning process, the substrates were dried in an oven at 60°C for 40 min and then treated with UV ozone for 20 min to eliminate any remaining residues on the ITO surface. The ZnO precursor sol-gel solution was prepared comprising of 219 mg of zinc acetate dehydrate [$Zn(CH_3CO_2)_2{\cdot}2H_2O$], 2 ml of 2-methoxyethanol ($C_3H_5O_2$), and 80 mg of ethanolamine ($HOCH_2CH_2NH_2$). After stirring the mixture for 5 min, the ZnO solution was sonicated for 30 min at 50°C and filtered through a 0.22-μm polyvinylidene difluoride filter. P3HT with a regioregularity of 95.7% and a molecular weight of 57467 g mol^{-1} (Ossila) was prepared in a 1,2-dichlorobenzene solution with optimized concentrations of 20 mg ml^{-1} and stirred at 50°C overnight. Ruthenium(III) chloride hydrate ($RuCl_3{\cdot}H_2O$) with a molecular weight of 207.43 g mol^{-1} was purchased from Sigma-Aldrich. An aqueous solution with a concentration of 0.01 M $RuCl_3{\cdot}H_2O$ was prepared to facilitate the electrochemical deposition of RuO_2.

For the fabrication of the RuO_2-integrated ZnO NW/$AgBiS_2$ NC–based biointerface, the process began with spin-coating the ZnO precursor sol-gel solution onto ITO substrates at a speed of 2000 rpm for 60 s. During this step, one-half of the substrate was carefully cleaned by softly wiping it with cotton swabs soaked in ethanol. Subsequently, the substrates were subjected to annealing, with glass/ITO substrates being exposed to a temperature of 275°C for 15 min, while PET/ITO substrates were annealed at 200°C for a duration of 30 min. ZnO NWs were synthesized via chemical bath deposition on an ITO/ZnO seed layer by dipping half of the substrate in ZnO NW. Following the formation of ZnO NWs on the ZnO seed layer, an annealing process was performed at a temperature of 200°C for 20 min. To precisely control the thickness of the interdigitated photoactive layers, the layer-by-layer deposition technique was used on half of the substrate during the fabrication process. This technique used a dip coating machine, enabling the accurate application of each layer to attain the desired thickness. Consequently, the dip coating method was used to infiltrate the ZnO NWs with a toluene solution containing $AgBiS_2$ NCs at a concentration of 20 g/liter. Following the infiltration of the $AgBiS_2$ NC photoactive layer, the introduction of TMAI-methanol (1 g/liter) was carried out to enhance the electronic coupling among the NCs by substituting the insulating oleate ligands with iodide ions. Subsequently, a methanol solution was used to rinse the substrates, aiming to remove excess oleic acid and TMAI ligands. This was succeeded by an annealing process at 110°C for a duration of 10 min. Afterward, the photoactive layer was formed by spin-coating the P3HT solution onto the ZnO NW/$AgBiS_2$ NC interdigitated layer at 1500 rpm for 60 s. Then, half of the substrate was cleaned by gently wiping it with cotton swabs soaked in toluene. Following these procedures, the photoactive segment of the neural interface is established on one half of the device, while the other half retained unmodified ITO. For the formation of the RuO_2 return anode electrode on the unaffected ITO section, the RuO_2 layer was electrodeposited via cyclic voltammetry (CV) by immersing the ITO return electrode region into a 0.01 M aqueous solution of $RuCl_3{\cdot}H_2O$ at room temperature, and CV was performed for 40 cycles with a scan rate of 50 mV s^{-1} from −0.2 to 1.2 V with respect to the Ag/AgCl bath electrode. Later, the devices underwent a rinse in distilled water and were then annealed at 50°C for 15 min.

Characterization of the biointerface

High-resolution imaging of the NW array–based biointerface was performed using a Zeiss Ultra Plus field-emission scanning electron microscope. Cross-sectional micrographs of the samples, both before and after layer-by-layer deposition, were obtained to characterize the surface morphology of the ZnO NWs, $AgBiS_2$ NC films, and interdigitated active layers. All samples were examined under an accelerating voltage of 10 kV and a working distance of 3.8 to 4.1 mm. A thin gold layer (a few nanometers thick) was sputter-coated onto the device surface to mitigate sample charging during scanning electron microscope analysis.

Chronoamperometry and chronopotentiometry measurements

For the photoelectrochemical measurements, including chronopotentiometry, chronoamperometry, electrochemical impedance spectroscopy, and cyclic voltammetry, an Autolab Potentiostat Galvanostat PGSTAT system (Metrohm, The Netherlands) was used. A three-electrode system was used, comprising a platinum rod counter electrode, a Ag/AgCl reference electrode, and the ITO layer of the biointerface as the working electrode. A precisely 1-cm^2 substrate area of the biointerface was defined and immersed, along with the other two electrodes, in extracellular aCSF as the electrolyte medium at room temperature to simulate the in vivo environment. A red light-emitting diode (LED) was used as a light source. Data acquisition and analysis were conducted using NOVA software. The optical power density of the applied light illumination on the biointerface was measured with an optical power meter (Newport 843-R). Measurements are the average of three independent measurements taken from 10 separate devices, and the shaded regions indicate the standard deviation of these measurements.

FDTD simulations

To elucidate the physical origin behind the absorption enhancement via the use of ZnO NWs, we performed FDTD simulations and compared the results with experimental outcomes. In the FDTD simulations, we used a simulation cell containing a single ZnO NW, where periodic boundary conditions were applied along the *xy* plane to model the array behavior, and a perfectly matched layer

Downloaded from https://www.science.org at Koc Universitesi Suna Kirac on July 02, 2026

boundary condition was used along the direction of the illumination light source (z axis). Figure S12 shows the refractive index properties of the materials used in the FDTD simulation (*38*, *39*). Figure S11 shows the experimental and calculated absorption spectra for different dip coating cycles in the presence (dashed curves) and absence (solid curves) of ZnO NWs, demonstrating their excellent correlation.

Photocurrent measurements

Measurements were conducted using an Olympus T2 upright microscope and EPC-800 patch clamp amplifiers (HEKA Elektronik GmbH, Pfalz, Germany). The aCSF medium was prepared by mixing 10 mM 4-(2 hydroxyethyl)-1-piperazineethanesulfonic acid (Hepes), 10 mM glucose, 2 mM $CaCl_2$, 140 mM NaCl, 1 mM $MgCl_2$, 3 mM KCl, and distilled water. The pH of the aCSF medium was adjusted to 7.4 using a stoichiometric amount of NaOH solution. A red LED (M780LP1, Thorlabs) was used as the light source, driven by a pulse-modulated LED driver (DC2200-High-Power 1-Channel, Thorlabs) to generate 20-ms light pulses. The electrolyte solution was grounded to simulate a biological environment, while the ITO layer remained ungrounded. Photocurrent measurements were then conducted.

Spatial selectivity of the device

The spatial selectivity of the devices was assessed by directly measuring the interfacial photocurrent at the electrode-electrolyte interface. The device was illuminated with a light spot size of 100 μm, and the resulting photocurrent spread was mapped by moving the patch pipette across the active area. The obtained values were then normalized.

Passive accelerated aging test

The long-term stability of the device was evaluated using an accelerated aging test. The passive accelerated aging test was performed by placing the devices in a glass petri dish filled with a H_2O_2-supplemented aCSF solution and incubating them at 87°C in a dry oven under dark conditions. This temperature corresponds to an acceleration factor of 32, calculated as $f = 2^{(\Delta t/10)}$ where $\Delta t = 87°C - 37°C$, assuming a body temperature of 37°C. The total aging duration was 576 hours to simulate 24 months. Charge injection performance was assessed at 48-hour intervals (simulating 2-month periods) throughout the test.

Low-temperature sterilization protocol

The low-temperature sterilization protocol of the device consisted of the following sequential steps: (i) a 5-min rinse in 70% ethanol, (ii) exposure to UV light for 30 min, (iii) incubation in a poly-L-lysine (Sigma-Aldrich, MO, US) solution for 1 hour at room temperature followed by overnight sterilization in cell culture medium at 37°C in a 5% CO_2 atmosphere for 24 hours, and (iv) a second 5-min rinse in 70% ethanol.

Primary neuron isolation

All experimental procedures have been approved by the Institutional Animal Care and Use Committees of Koç University (approval no. 2022.HADYEK.048) according to Directive 2010/63/EU of the European Parliament and of the Council on the Protection of Animals Used for Scientific Purposes. The hippocampal tissue was isolated from the brains of embryos of Wistar Albino rats on embryonic days 16 to 18. The tissue was put directly into ice-cold Hank's balanced salt solution (HBSS) including a Falcon tube. After taking the Falcon tube to the sterilized cell culture hood, the tissue was washed two times with sterile ice-cold Hank's balanced salt solution. Then, a 0.25% trypsin-EDTA solution with 2% deoxyribonuclease I supplement was added to the tissue for a 20-min incubation in a 37°C water bath for enzymatic digestion. During this time, the tube was made upside down for better digestion. Afterward, Dulbecco's modified Eagle's medium/nutrient mixture F-12 (DMEM/F12) supplemented with 10% fetal bovine serum and 1% penicillin/streptomycin was added and centrifuged at 300*g* for 3 min. After the centrifugation, DMEM/F12 was carefully discarded, and the tissue was washed two times with DMEM/F12. After discarding the DMEM/F12, Neurobasal Plus medium supplemented with B27, L-glutamine, β-mercaptoethanol, glutamate, and 1% penicillin/streptomycin was added to the cell pellet and triturated with plastic Pasteur pipette for homogenizing the cells. The mixed solution was dissociated through a 70-μm cell strainer.

Then, 500,000 cells per well were seeded to each substrate. The well plate was put in the 37°C cell culture incubator with 5% CO_2 and incubated for 3 days unmoved. On the third day, half of the medium of the cells was changed with the Neurobasal medium (NBM)–supplemented cytosine arabinoside to inhibit the overgrowth of glial cells and then incubated for 24 hours in a cell culture incubator. The next day, the entire medium was replaced with NBM supplemented with B27, L-glutamine, and 1% penicillin/streptomycin. Until use in the experiments, half of the culture medium was replaced with fresh NBM every 3 to 4 days.

CTG luminescent cell viability assay

CTG Luminescent Cell Viability Assay (Promega, Mannheim, Germany) was used to examine the viability of primary hippocampal neurons on the surface of ITO and fabricated devices. On day 0, the well plate was taken from the incubator and left at room temperature for 30 min. Then, CTG Reagent was added to each well, and the plate was put on the orbital shaker for 5 min and incubated at room temperature for 10 min for stabilization of luminescence signals. Then, each solution inside the wells was transferred to a 96-well opaque plate. A Synergy H1 Microplate Reader (Bio-Tek Instruments) was used to measure the luminescence signals. The relative cell viability of samples of each substrate was calculated from comparing luminescence signals (relative light units) of fabricated devices with the ones of ITO control.

MTT cytotoxicity assay

MTT cytotoxicity assay was performed to analyze cell viability on the basis of the reduction of a yellow tetrazolium salt (MTT) to purple formazan crystals by metabolically active cells. At day 0, Neurobasal Plus medium supplemented with B27, L-glutamine, and 1% penicillin/streptomycin in the wells was replaced with Neurobasal Plus medium including an MTT solution (5 mg/ml; Thermo Fisher Scientific, MA, US). The culture plate was incubated at 37°C and 5% CO_2 in a cell culture incubator for 4 hours. After the incubation, all substrates were taken to a new six-well plate, and a 1:1 mixture of dimethyl sulfoxide and ethanol was added to the samples for solubilizing the formazan salts and incubated at 37°C for 10 min. Then, the solution in each well was transferred to a 96-well plate. The Synergy H1 Microplate Reader (Bio-Tek Instruments) was used to measure the absorbance at a 570-nm wavelength. The relative cell viability of each substrate was calculated normalizing the control ITO as follows: Viability = $(OD_{sample}/OD_{control}) \times 100$. The optical density (OD) of the sample was obtained from the cells grown on the fabricated device, and the OD of control was obtained from the cells grown on the ITO.

Downloaded from https://www.science.org at Koc Universitesi Suna Kirac on July 02, 2026

LDH release assay

For the LDH release assay, the CytoSelect LDH Cytotoxicity Assay Kit (CBA-241, Cell Biolabs) was used to examine the cell membrane stability of primary neuronal cells cultured on the samples. As a positive control of the experiment, the cells on the ITO substrates were incubated with culture medium containing 1% Triton X-100 for 10 min at 37°C in a 5% CO_2 cell culture incubator to induce LDH leakage. All experimental and control groups were incubated with the medium including 1% water for 10 min, and then 90 μl of culture medium was taken from each sample and added to transparent 96-well cell culture plates. Thereafter, 10 μl of LDH cytotoxicity assay reagent was added to each well, and the plates were incubated at 37°C in a 5% CO_2 incubator for 30 min to allow the reaction to occur. The Synergy H1 Microplate Reader (BioTek) device was used to measure the amount of LDH leaked into the culture medium at 450-nm OD.

Immunofluorescence staining and imaging

On day 0, the samples of substrates were fixed with 4% paraformaldehyde for 20 min in a fume hood and washed three times with PBS-T (phosphate-buffered saline and 0.1% Tween 20). Then, 0.1% Triton X-100 was added to the samples and incubated for 8 min for permeabilization following washing with PBS-T. The superblock was used to perform blocking for 10 min at room temperature. The samples were incubated at 4° overnight with a rabbit anti-NeuN antibody (ab177487, Abcam, Cambridge, UK) and an anti–β-III tubulin antibody (ab18207, Abcam, Cambridge, UK), all prepared in the superblock. After incubation, the samples were washed three times with PBS-T. For anti-NeuN and anti–β-III tubulin labeling, the samples were incubated with goat anti-rabbit IgG H&L Alexa Fluor 488 (Cell Signaling Technology, MA, US) for 90 min at 37°C. After the incubation, all samples were washed three times using PBS-T and mounted with a DAPI (4′,6-diamidino-2-phenylindole)–supplemented mounting medium (50001, Ibidi GmbH, Germany). All immunofluorescence images were taken by an inverted fluorescence light microscope (Axio Observer Z1, ZEISS, Oberkochen, Germany). For day 14 experiments, the same procedure was established on the 14th day of culture.

Intracellular oxidative stress measurement

The intracellular oxidative stress level was measured by the cellular ROS assay kit 2′,7′-dichlorodihydrofluorescein diacetate (H_2DFC-DA) (ab113851, Abcam). Primary hippocampal neurons were seeded on the control and device as 500,000 cells per well and cultured until 14 days in vitro. Experimental groups included ITO control, the device before and after illumination, and positive control with neurons grown on the control substrate treated with 100 μM H_2O_2 for 30 min. For the experiment, cells were washed once with PBS and then incubated with 20 μM H_2DFCDA in a live-cell solution for 45 min before imaging at 37°C and 5% CO_2. Hoechst (0.6 mg/ml) was used to stain the nucleus before imaging for 15 min. After incubation, cells were washed twice with PBS and then incubated with a live-cell solution for 10 min at room temperature to stabilize the signals. All immunofluorescence images were taken in the same light intensity, exposure, time point, and magnification with a live-cell fluorescence microscope (Axio Observer Z1, ZEISS, Oberkochen, Germany), and the average fluorescence intensity was measured by Zen Blue 3.5 software. The light stimulation group was prepared with exposure of 780-nm light with 10,000 cycles and illumination at a 5-Hz stimulus frequency, 20-ms pulse width, and 1.5 mW mm^{-2} optical power density. The fluorescence intensity of ITO control was accepted as 100% in relative fluorescence intensity comparison.

MMP assay

MMP was analyzed using the JC-1 assay (T3168, Invitrogen), in accordance with the manufacturer's protocol. Briefly, primary hippocampal neurons were seeded onto the control and device as 500,000 cells per well and cultured for 5 to 7 days. The cells were stained with 1 μM JC-1 prepared in a live-cell solution (Invitrogen, cat. no. A59688DJ) at 37°C and incubated for 30 min in the dark. They were then washed twice with PBS to remove excess dye, and JC-1 fluorescence was observed via a confocal laser scanning microscope (DMI8 SP8, Leica, Wetzlar, Germany). Cells were subjected to 780-nm light for 20 s with a 5-Hz stimulus frequency, 20-ms pulse width, and 1.5 mW mm^{-2} optical power density. The mean fluorescence intensity of the JC-1 red aggregate and JC-1 green monomer was quantified and processed using LASX software (Leica, Germany).

Rat retina preparation, electrophysiological recording, and NIR stimulation

Experiments were conducted in accordance with the National Institutes of Health Guide for the Care and Use of Laboratory Animals. Studies were approved by the Local Animal Ethics Committee and conducted in agreement with Directive 2010/63/EU of the European Parliament. P23H male transgenic rats (>9 months) were raised locally.

Using a custom 3D-printed descender, an implant (photovoltaic device of ~2 by 2mm) was positioned on the center of a filter membrane (Whatman, GE Healthcare Life Sciences). Retinal pieces were then flattened on the membrane, entirely covering the implant, and then gently pressed against an MEA (electrode diameter, 30 μm; spacing, 100 μm; MEA256 100/30 iR-ITO, MultiChannel Systems) with the RGCs facing the electrodes. The retinal tissue was continuously perfused with Ames' medium (Sigma-Aldrich) bubbled with 95% O_2 and 5% CO_2 at 35°C at a rate of 3 ml min^{-1}. RGC recordings were obtained with a 252-channel preamplifier and MC_Rack version 4.6.2 software (MultiChannel Systems).

We observed that the tighter the contact between the implant and the retina was, the more current generated by the implant was transmitted to the retina (visible in MEA recordings in the form of larger artifacts, with a positive saturating amplitude >2 mV). However, on the other hand, the stronger the contact, the greater the risk of hypoxia for the retina, causing a potential rapid loss (in the minute range) of spiking spontaneous activity and light responses. We used for all experiments an output light power density of 2.27 mW mm^{-2} to maximize the effect of the implant without having to press too much the implant on the retina.

Raw extracellular recordings were acquired from a 256-channel MEA, and .MCD raw data files were exported to .HDF5 file format and processed using a Butterworth bandpass filter (300 to 2000 Hz) to isolate neuronal spiking activity. Electrical artifacts were detected and averaged across occurrences to compute an artifact template, which was subtracted from the raw signal to significantly remove NIR stimulation–induced distortions. Spikes were detected using the first derivative of the artifact-cleaned signal, selecting negative peaks exceeding an adaptive threshold (−4.5 × SD). Events occurring within saturating laser artifact windows were excluded, with a margin of ~1 ms before and after the artifact to ensure robust detection. No spike sorting was performed because recordings were generally not stable enough or too short; therefore, the activity of

Downloaded from https://www.science.org at Koc Universitesi Suna Kirac on July 02, 2026

individual MEA units may reflect the combined activity of multiple RGCs.

MEA units were classified as active if their mean firing rate exceeded a predefined threshold (e.g., 0.5 Hz) during a control period of spontaneous activity. Responsive units were detected on the basis of the calculation of spike density function (SDF) using Gaussian smoothing and determination of the peak response within a predefined time window following the stimulation onset. A unit was classified as responsive if the peak SDF or "peak firing rate" exceeded 4.5 × SD of baseline activity. Latencies were calculated as the time between the stimulus onset and the time of the SDF peak. Spatial heatmaps and smoothed temporal heatmaps were generated to illustrate network-wide activation patterns. For spatial heatmap representation (normalized firing rates), only active units were color coded between 0 and 1, with dark blue (value 0) corresponding to active but nonresponsive units and pure yellow (value 1) corresponding to the unit presenting the maximum response. Data were filtered, cleaned, and analyzed with custom scripts written in MATLAB (MathWorks 2023a).

Light stimuli were delivered with a single-mode NIR laser source (880 nm, 2.5 W, Laser 2000) coupled to a digital micromirror device (Vialux; resolution, 1024 by 768) and a 4× objective using an inverted microscope. The implant was stimulated through the MEA and the retina. Recording sessions consisted of 100 repetitions at 5 Hz of short NIR laser stimulations (period of 200 ms). Different stimulation pulse widths were tested: 5, 10, 20, and 50 ms. Output power density was measured with a power meter sensor (sensor S121C, Thorlabs) positioned at the level of the retinal explant.

Optical safety considerations

The maximum permissible radiant power (MP) for chronic retinal exposure is determined in accordance with established eye safety standards (*18*). In the NIR region, the photochemical damage limit is not applicable. For photothermal and photoacoustic limits, the MP is calculated using the equation $MP = 6.93 \times 10^{-5} C_T C_E P^{-1}$, where $C_T = 10^{0.002\,(\lambda - 700)}$. Here, the pupil factor (P) equals 1 between 700- and 1400-nm wavelengths of light. A retinal spot size larger than 1.7 mm, on the basis of a previous study (*40*), is taken as 29.3 W mm^{-2}. For single-pulse exposures with durations ranging from 0.05 to 70 ms, the limit is given by $MP_{single} = 6.93 \times 10^{-4} C_T C_E t^{-0.25}$. While these equations provide average irradiance limits, the peak irradiance limits (MP_{peak}) can be derived using the formula $MP_{avg}/(txf)$, where t is the pulse duration, and f is the pulse frequency.

Supplementary Materials

This PDF file includes:

Figs. S1 to S20
Table S1
References

REFERENCES

1. F. Patolsky, B. P. Timko, G. Yu, Y. Fang, A. B. Greytak, G. Zheng, C. M. Lieber, Detection, stimulation, and inhibition of neuronal signals with high-density nanowire transistor arrays. *Science* **313**, 1100–1104 (2006).
2. J. Liu, T.-M. Fu, Z. Cheng, G. Hong, T. Zhou, L. Jin, M. Duvvuri, Z. Jiang, P. Kruskal, C. Xie, Z. Suo, Y. Fang, C. M. Lieber, Syringe-injectable electronics. *Nat. Nanotechnol.* **10**, 629–636 (2015).
3. T.-M. Fu, G. Hong, T. Zhou, T. G. Schuhmann, R. D. Viveros, C. M. Lieber, Stable long-term chronic brain mapping at the single-neuron level. *Nat. Methods* **13**, 875–882 (2016).
4. J. Shi, C. Sun, E. Liang, B. Tian, Semiconductor nanowire-based cellular and subcellular interfaces. *Adv. Funct. Mater.* **32**, 2107997 (2022).
5. A. Zhang, J.-H. Lee, C. M. Lieber, Nanowire-enabled bioelectronics. *Nano Today* **38**, 101135 (2021).
6. J. Deng, Y. Su, D. Liu, P. Yang, B. Liu, C. Liu, Nanowire photoelectrochemistry. *Chem. Rev.* **119**, 9221–9259 (2019).
7. P. Krogstrup, H. I. Jørgensen, M. Heiss, O. Demichel, J. V. Holm, M. Aagesen, J. Nygard, A. Fontcuberta i Morral, Single-nanowire solar cells beyond the Shockley–Queisser limit. *Nat. Photonics* **7**, 306–310 (2013).
8. R. Parameswaran, J. L. Carvalho-de-Souza, Y. Jiang, M. J. Burke, J. F. Zimmerman, K. Koehler, A. W. Phillips, J. Yi, E. J. Adams, F. Bezanilla, B. Tian, Photoelectrochemical modulation of neuronal activity with free-standing coaxial silicon nanowires. *Nat. Nanotechnol.* **13**, 260–266 (2018).
9. R. Parameswaran, K. Koehler, M. Y. Rotenberg, M. J. Burke, J. Kim, K.-Y. Jeong, B. Hissa, M. D. Paul, K. Moreno, N. Sarma, T. Hayes, E. Sudzilovsky, H.-G. Park, B. Tian, Optical stimulation of cardiac cells with a polymer-supported silicon nanowire matrix. *Proc. Natl. Acad. Sci. U.S.A.* **116**, 413–421 (2019).
10. C. Ronzani, T. Cottineau, I. Gonzalez-Valls, V. Keller, S. Picaud, N. Keller, M. J. Roux, High-frequency stimulation of normal and blind mouse retinas using TiO_2 nanotubes. *Adv. Funct. Mater.* **28**, 1804639 (2018).
11. D. R. Merrill, M. Bikson, J. G. R. Jefferys, Electrical stimulation of excitable tissue: Design of efficacious and safe protocols. *J. Neurosci. Methods* **141**, 171–198 (2005).
12. O. Karatum, M.-J. Gwak, J. Hyun, A. Onal, G. R. Koirala, T.-I. Kim, S. Nizamoglu, Optical neuromodulation at all scales: From nanomaterials to wireless optoelectronics and integrated systems. *Chem. Soc. Rev.* **52**, 3326–3352 (2023).
13. S. F. Cogan, Neural stimulation and recording electrodes. *Annu. Rev. Biomed. Eng.* **10**, 275–309 (2008).
14. J. Tang, N. Qin, Y. Chong, Y. Diao, Yiliguma, Z. Wang, T. Xue, M. Jiang, J. Zhang, G. Zheng, Nanowire arrays restore vision in blind mice. *Nat. Commun.* **9**, 786 (2018).
15. R. Yang, P. Zhao, L. Wang, C. Feng, C. Peng, Z. Wang, Y. Zhang, M. Shen, K. Shi, S. Weng, C. Dong, F. Zeng, T. Zhang, X. Chen, S. Wang, Y. Wang, Y. Luo, Q. Chen, Y. Chen, C. Jiang, S. Jia, Z. Yu, J. Liu, F. Wang, S. Jiang, W. Xu, L. Li, G. Wang, X. Mo, G. Zheng, A. Chen, X. Zhou, C. Jiang, Y. Yuan, B. Yan, J. Zhang, Assessment of visual function in blind mice and monkeys with subretinally implanted nanowire arrays as artificial photoreceptors. *Nat. Biomed. Eng.* **8**, 1018–1039 (2024).
16. A. Corna, K. Gugujonovic, M. Schiek, A. Bellapianta, P. Werginz, A. Ziller, M. C. Scharber, A. Salti, M. Bolz, M. Irimia-Vladu, G. Zeck, Near-infrared organic photovoltaic electrodes for subretinal neurostimulation. *Adv. Funct. Mater.* , e15327 (2025).
17. H. Cui, S. Zhao, G. Hong, Wireless deep-brain neuromodulation using photovoltaics in the second near-infrared spectrum. *Device* **1**, 100113 (2023).
18. F. C. Delori, R. H. Webb, D. H. Sliney, American National Standards Institute, Maximum permissible exposures for ocular safety (ANSI 2000), with emphasis on ophthalmic devices. *J. Opt. Soc. Am. A* **24**, 1250–1265 (2007).
19. S. Wang, C. Jiang, Y. Yu, Z. Zhang, R. Quhe, R. Yang, Y. Tian, X. Chen, W. Fan, Y. Niu, B. Yan, C. Jiang, Y. Wang, Z. Wang, C. Liu, W. Hu, J. Zhang, P. Zhou, Tellurium nanowire retinal nanoprosthesis improves vision in models of blindness. *Science* **388**, eadu2987 (2025).
20. X. Wu, Y. Jiang, N. J. Rommelfanger, F. Yang, Q. Zhou, R. Yin, J. Liu, S. Cai, W. Ren, A. Shin, K. S. Ong, K. Pu, G. Hong, Tether-free photothermal deep-brain stimulation in freely behaving mice via wide-field illumination in the near-infrared-II window. *Nat. Biomed. Eng.* **6**, 754–770 (2022).
21. S. L. Diedenhofen, M. Bernechea, K. M. Felter, F. C. Grozema, L. D. A. Siebbeles, Charge photogeneration and transport in $AgBiS_2$ nanocrystal films for photovoltaics. *Solar RRL* **3**, 1900075 (2019).
22. Y. Xiao, H. Wang, F. Awai, N. Shibayama, T. Kubo, H. Segawa, Eco-friendly $AgBiS_2$ nanocrystal/ZnO nanowire heterojunction solar cells with enhanced carrier collection efficiency. *ACS Appl. Mater. Interfaces* **13**, 3969–3978 (2021).
23. M. Bernechea, N. Cates, G. Xercavins, D. So, A. Stavrinadis, G. Konstantatos, Solution-processed solar cells based on environmentally friendly AgBiS2 nanocrystals. *Nat. Photonics* **10**, 521–525 (2016).
24. P.-H. Prévot, K. Gehere, F. Arcizet, H. Akolkar, M. A. Khoei, K. Blaize, O. Oubari, P. Daye, M. Lanoë, M. Valet, S. Dalouz, P. Langlois, E. Esposito, V. Forster, E. Dubus, N. Wattiez, E. Brazhnikova, C. Nouvel-Jaillard, Y. LeMer, J. Demilly, C.-M. Fovet, P. Hantraye, M. Weissenburger, H. Lorach, E. Bouillet, M. Deterre, R. Hornig, G. Buc, J.-A. Sahel, G. Chenegros, P. Pouget, R. Benosman, S. Picaud, Behavioural responses to a photovoltaic subretinal prosthesis implanted in non-human primates. *Nat. Biomed. Eng.* **4**, 172–180 (2020).
25. T. W. Huang, T. I. Kamins, Z. C. Chen, B.-Y. Wang, M. Bhuckory, L. Galambos, E. Ho, T. Ling, S. Afshar, A. Shin, V. Zuckerman, J. S. Harris, K. Mathieson, D. Palanker, Vertical-junction photodiodes for smaller pixels in retinal prostheses. *J. Neural Eng.* **18**, 036015 (2021).
26. H. Lorach, J. Wang, D. Y. Lee, R. Dalal, P. Huie, D. Palanker, Retinal safety of near infrared radiation in photovoltaic restoration of sight. *Biomed. Opt. Express* **7**, 13–21 (2016).
27. D. Palanker, Y. Le Mer, S. Mohand-Said, J. A. Sahel, Simultaneous perception of prosthetic and natural vision in AMD patients. *Nat. Commun.* **13**, 513 (2022).

Downloaded from https://www.science.org at Koc Universitesi Suna Kirac on July 02, 2026

28. F. G. Holz, Y. L. Mer, M. M. K. Muqit, L.-O. Hattenbach, A. Cusumano, S. Grisanti, L. Kodjikian, M. A. Pileri, F. Matonti, E. Souied, B. V. Stanzel, P. Szurman, M. Weber, K. U. Bartz-Schmidt, N. Eter, M. N. Delyfer, J. F. Girmens, K. A. van Overdam, A. Wolf, R. Hornig, M. Corazzol, F. Brodie, L. O. de Koo, D. Palanker, J.-A. Sahel, Subretinal photovoltaic implant to restore vision in geographic atrophy due to AMD. *N. Engl. J. Med.*, 10.1056/NEJMoa2501396 (2025).
29. A. Onal, T. S. Kaya, Ö. Metin, S. Nizamoglu, Emergence of near-infrared photoluminescence via ZnS shell growth on the $AgBiS_2$ nanocrystals. *Chem. Mater.* **37**, 255–265 (2024).
30. X.-g. Wu, Y. Jing, H. Zhong, In situ fabricated perovskite quantum dots: From materials to applications. *Adv. Mater.* **37**, e2412276 (2025).
31. B. T. Diroll, B. Guzelturk, H. Po, C. Dabard, N. Fu, L. Makke, E. Lhuillier, S. Ithurria, 2D II–VI semiconductor nanoplatelets: From material synthesis to optoelectronic integration. *Chem. Rev.* **123**, 3543–3624 (2023).
32. S. Rowland, A. Aghakhani, R. D. Whalley, A. M. Ferreira, N. Kotov, P. Gentile, Layer-by-layer nanoparticle assembly for biomedicine: Mechanisms, technologies, and advancement via acoustofluidics. *ACS Appl. Nano Mater.* **7**, 15874–15902 (2024).
33. R. Balamur, T. S. Kaya, S. Sariyer, H. N. Kaleli, A. Onal, U. B. Caliskan, M. Hasanreisoğlu, R. Demir-Cakan, S. Nizamoglu, Biointerfacing with $AgBiS_2$ quantum dots for pseudocapacitive photostimulation. *Adv. Funct. Mater.* **35**, 2422083 (2025).
34. V. L. S. dos Santos, R. C. Araújo, E. S. Lisboa, A. M. Lopes, R. L. de Albuquerque-Júnior, J. C. Cardoso, C. Blanco-Llamero, T. A. Deshpande, H. O. W. Anderson, R. Priefer, E. B. Souto, P. Severino, Layer-by-layer assembly: A versatile approach for tailored biomedical films and drug delivery. *J. Drug Deliv. Sci. Technol.* **91**, 105243 (2024).
35. P. Li, J. Zhang, H. Hayashi, J. Yue, W. Li, C. Yang, C. Sun, J. Shi, J. Huberman-Shlaes, N. Hibino, B. Tian, Monolithic silicon for high spatiotemporal translational photostimulation. *Nature* **626**, 990–998 (2024).
36. A. Prominski, J. Shi, P. Li, J. Yue, Y. Lin, J. Park, B. Tian, M. Y. Rotenberg, Porosity-based heterojunctions enable leadless optoelectronic modulation of tissues. *Nat. Mater.* **21**, 647–655 (2022).
37. O. F. Ozelci, H. N. Kaleli, T. S. Kaya, G. Yildiz, M. Oztopal, E. Sarıoğlu, E. Ödemiş, E. Senses, S. Nizamoglu, Hydrogel-integrated quantum dot biointerfaces for near-infrared cardiac photostimulation. *Adv. Funct. Mater.* , e13988 (2025).
38. J. J. Cheng, C.-H. M. Chuang, O. Hentz, P. H. Rekemeyer, M. G. Bawendi, S. Gradečak, Dimension- and surface-tailored ZnO nanowires enhance charge collection in quantum dot photovoltaic devices. *ACS Appl. Energy Mater.* **1**, 1815–1822 (2018).
39. Y. Wang, S. R. Kavanagh, I. Burgués-Ceballos, A. Walsh, D. O. Scanlon, G. Konstantatos, Cation disorder engineering yields $AgBiS_2$ nanocrystals with enhanced optical absorption for efficient ultrathin solar cells. *Nat. Photonics* **16**, 235–241 (2022).
40. K. Mathieson, J. Loudin, G. Goetz, P. Huie, L. Wang, T. I. Kamins, L. Galambos, R. Smith, J. S. Harris, A. Sher, D. Palanker, Photovoltaic retinal prosthesis with high pixel density. *Nat. Photonics* **6**, 391–397 (2012).
41. R. Balamur, J. T. Oh, O. Karatum, Y. Wang, A. Onal, H. N. Kaleli, C. Pehlivan, A. Şahin, M. Hasanreisoglu, G. Konstantatos, S. Nizamoglu, Capacitive and efficient near-infrared stimulation of neurons via an ultrathin $AgBiS_2$ nanocrystal layer. *ACS Appl. Mater. Interfaces* **16**, 29610–29620 (2024).
42. O. Karatum, H. N. Kaleli, G. O. Eren, A. Sahin, S. Nizamoglu, Electrical stimulation of neurons with quantum dots via near-infrared light. *ACS Nano* **16**, 8233–8243 (2022).
43. M. J. I. Airaghi Leccardi, N. A. L. Chenais, L. Ferlauto, M. Kawecki, E. G. Zollinger, D. Ghezzi, Photovoltaic organic interface for neuronal stimulation in the near-infrared. *Commun. Mater.* **1**, 21 (2020).
44. M. Silverå Ejneby, M. Jakešová, J. J. Ferrero, L. Migliaccio, I. Sahalianov, Z. Zhao, M. Berggren, D. Khodagholy, V. Đerek, J. N. Gelinas, E. D. Głowacki, Chronic electrical stimulation of peripheral nerves via deep-red light transduced by an implanted organic photocapacitor. *Nat. Biomed. Eng.* **6**, 741–753 (2022).
45. L. Ferlauto, M. J. I. Airaghi Leccardi, N. A. L. Chenais, S. C. A. Gilliéron, P. Vagni, M. Bevilacqua, T. J. Wolfensberger, K. Sivula, D. Ghezzi, Design and validation of a foldable and photovoltaic wide-field epiretinal prosthesis. *Nat. Commun.* **9**, 992 (2018).
46. O. Karatum, E. Yildiz, H. N. Kaleli, A. Sahin, B. Ulgut, S. Nizamoglu, RuO_2 supercapacitor enables flexible, safe, and efficient optoelectronic neural interface. *Adv. Funct. Mater.* **32**, 2109365 (2022).
47. M. Han, S. B. Srivastava, E. Yildiz, R. Melikov, S. Surme, I. B. Dogru-Yuksel, I. H. Kavakli, A. Sahin, S. Nizamoglu, Organic photovoltaic pseudocapacitors for neurostimulation. *ACS Appl. Mater. Interfaces* **12**, 42997–43008 (2020).
48. M. Han, H. Bahmani Jalali, E. Yildiz, M. H. Qureshi, A. Şahin, S. Nizamoglu, Photovoltaic neurointerface based on aluminum antimonide nanocrystals. *Commun. Mater.* **2**, 19 (2021).
49. O. Karatum, M. M. Aria, G. O. Eren, E. Yildiz, R. Melikov, S. B. Srivastava, S. Surme, I. B. Dogru, H. Bahmani Jalali, B. Ulgut, A. Sahin, I. H. Kavakli, S. Nizamoglu, Nanoengineering InP quantum dot-based photoactive biointerfaces for optical control of neurons. *Front. Neurosci.* **15**, 652608 (2021).

Acknowledgments: We express gratitude to the Koç University Research Center for Translational Medicine (KUTTAM) for providing access to its services and facilities, supported by funding from the Republic of Turkey Ministry of Development. The content is solely the responsibility of the authors and does not necessarily represent the official views of the Ministry of Development. We acknowledge B. Yagcı from the Koç University Surface Science and Technology Center (KUYTAM) for conducting the scanning electron microscopy and XPS measurements. We also thank G. S. Franci for assistance in FTIR characterization. We are grateful to G. Corapcioglu from the Koç University Nanofabrication and Nanocharacterization Center for Scientific and Technological Advanced Research for providing TEM and high-resolution TEM imaging. In addition, we thank the Koç University Boron and Advanced Materials Application and Research Center (KUBAM) for performing the XRD analysis. **Funding:** This work was funded by the European Union (ERC, MESHOPTO; grant ID: 101045289). The views and opinions expressed in this paper are solely those of the authors only and do not necessarily reflect those of the European Union or the European Research Council Executive Agency. Neither the European Union nor the granting authority can be held responsible for these views. This work was also supported by IHU FOReSIght, by DIM C-BRAINS and Région Ile-de-France, and by ERC grant (NeuroSonoGene, 101118744), funded by the European Union. Views and opinions expressed are however those of the author(s) only and do not necessarily reflect those of the European Union or the European Research Council Executive Agency. Neither the European Union nor the granting authority can be held responsible for them. G.Z. and A.Co. also acknowledge financial support from Hochschuljubiläumsfonds der Stadt Wien (H-864102/2022). **Author contributions:** Conceptualization: S.N. Investigation: S.N., T.S.K., H.N.K., and A.Ch. Data curation: T.S.K., H.N.K., A.Ch., and C.P. Methodology: T.S.K., H.N.K., A.Ch., C.J., R.B., U.B.C., A.O., and S.N. Formal analysis: T.S.K., H.N.K., A.Ch., C.J., C.P., and A.E.C. Visualization: T.S.K., H.N.K., A.Ch., A.E.C., and S.N. Writing—original draft: T.S.K., H.N.K., A.Ch., A.Co., C.J., C.P., and S.N. Writing—review and editing: T.S.K., H.N.K., A.Ch., A.Co., C.J., U.B.C., E.T., A.Y., R.M., A.E.C., and S.N. Supervision: G.Z., S.P., and S.N. **Competing interests:** The authors declare that they have no competing interests. **Data and materials availability:** All data and code needed to evaluate and reproduce the results in the paper are present in the paper and/or the Supplementary Materials.

Submitted 18 July 2025
Accepted 24 December 2025
Published 21 January 2026
10.1126/sciadv.aea7001

Downloaded from https://www.science.org at Koc Universitesi Suna Kirac on July 02, 2026

Science Advances

Photovoltaic nanoassembly of nanowire arrays sensitized with colloidal nanocrystals for near-infrared retina photostimulation

Tarik S. Kaya, Humeyra N. Kaleli, Antoine Chaffiol, Andrea Corna, Corentin Joffrois, Ridvan Balamur, Ugur B. Caliskan, Asim Onal, Cigdem Pehlivan, Eren Tekinay, Alp Yilmaz, Roya Mohajeri, Arif E. Cetin, Günther Zeck, Serge Picaud, and Sedat Nizamoglu

Sci. Adv. **12** (4), eaea7001. DOI: 10.1126/sciadv.aea7001

View the article online
https://www.science.org/doi/10.1126/sciadv.aea7001
Permissions
https://www.science.org/help/reprints-and-permissions

Downloaded from https://www.science.org at Koc Universitesi Suna Kirac on July 02, 2026

Use of this article is subject to the Terms of service

Science Advances (ISSN 2375-2548) is published by the American Association for the Advancement of Science. 1200 New York Avenue NW, Washington, DC 20005. The title *Science Advances* is a registered trademark of AAAS.

Copyright © 2026 The Authors, some rights reserved; exclusive licensee American Association for the Advancement of Science. No claim to original U.S. Government Works. Distributed under a Creative Commons Attribution NonCommercial License 4.0 (CC BY-NC).